

# Determination of the infrared complex magneto-conductivity tensor in itinerant ferromagnets from Faraday and Kerr measurements

M.-H. Kim,<sup>1</sup> G. Acbas,<sup>1</sup> M.-H. Yang,<sup>1</sup> I. Ohkubo,<sup>2</sup> H. Christen,<sup>3</sup> D. Mandrus,<sup>3</sup>  
M.A. Scarpulla,<sup>4</sup> O.D. Dubon,<sup>4</sup> Z. Schlesinger,<sup>5</sup> P. Khalifah,<sup>6</sup> and J. Cerne<sup>1</sup>

<sup>1</sup>*Department of Physics, University at Buffalo, SUNY, Buffalo, NY 14260, USA*

<sup>2</sup>*Department of Applied Chemistry, Univ. of Tokyo, Tokyo, Japan*

<sup>3</sup>*Oak Ridge National Laboratory, Materials Science and Technology Division, Oak Ridge, TN 37831, USA*

<sup>4</sup>*Department of Materials Science and Engineering, and Lawrence Berkeley National Laboratory, University of California, Berkeley, CA 94720, USA*

<sup>5</sup>*Department of Physics, University of California, Santa Cruz, CA 95064, USA and*

<sup>6</sup>*Department of Chemistry, University of Massachusetts, Amherst, MA 01003, USA*

(Dated: cond-mat/0701158, submitted to Phys. Rev. B, January 2007)

## Abstract

We present measurement and analysis techniques that allow the complete complex magneto-conductivity tensor to be determined from mid-infrared (11-1.6  $\mu\text{m}$ ; 100-800 meV) measurements of the complex Faraday ( $\theta_F$ ) and Kerr ( $\theta_K$ ) angles. Since this approach involves measurement of the geometry (orientation axis and ellipticity of the polarization) of transmitted and reflected light, no absolute transmittance or reflectance measurements are required. Thick film transmission and reflection equations are used to convert the complex  $\theta_F$  and  $\theta_K$  into the complex longitudinal conductivity  $\sigma_{xx}$  and the complex transverse (Hall) conductivity  $\sigma_{xy}$ .  $\theta_F$  and  $\theta_K$  are measured in a  $\text{Ga}_{1-x}\text{Mn}_x\text{As}$  and  $\text{SrRuO}_3$  films. The resulting  $\sigma_{xx}$  is compared to the values obtained from conventional transmittance and reflectance measurements, as well as the results from Kramers-Kronig analysis of reflectance measurements on similar films.

## I. INTRODUCTION

Conventional dc Hall effect measurements have been essential in revealing the unusual character of novel electronic materials including high temperature superconducting cuprates (HTSC),<sup>1</sup> diluted magnetic semiconductors (DMS),<sup>2</sup> and ruthenate perovskite (RP)<sup>3,4</sup> materials. In many of these materials, the Hall angle  $\theta_H$  and transverse (Hall) conductivity  $\sigma_{xy}$  provide information critical to understanding their electronic properties. The frequency dependence of  $\theta_H$  and  $\sigma_{xy}$  is very sensitive to the electronic structure, and in many cases exposes new insights that are hidden from the longitudinal conductivity  $\sigma_{xx}$  that is measured by conventional spectroscopy. The mid-infrared (MIR: 11-1.6  $\mu\text{m}$ ; 100-800 meV) energy range is particularly interesting in many of these materials. For example, the band structure of RP<sup>5</sup> and III-V(Mn) DMS<sup>6,7</sup> leads to predictions of strong spectral features in  $\sigma_{xy}$  in the MIR. In the electron-doped cuprate,  $\text{Pr}_{2-x}\text{Ce}_x\text{CuO}_4$ , evidence of a spin density wave gap has been observed in the MIR behavior of  $\sigma_{xy}$ .<sup>8</sup>

Reflection and transmission magneto-polarimetry measurements allow one to determine the complex Faraday  $\theta_F$  and Kerr  $\theta_K$  angles, respectively.  $\theta_F$  ( $\theta_K$ ) describes the change in polarization of transmitted (reflected) light produced by a sample in a magnetic field. Although,  $\theta_F$  and  $\theta_K$  are useful, they depend on the optical geometry of the sample, such as the thickness of the film and index of refraction of the substrate. Furthermore, calculations of  $\theta_F$  and  $\theta_K$  depend on which assumptions are made for the optical formulas, e.g., thin film, thick film, and bulk. Theoretical models typically calculate response functions such as  $\sigma_{xy}$  and  $\sigma_{xx}$ . Since these conductivities are related to the electronic behavior in a more fundamental way, it is useful to convert  $\theta_F$  and  $\theta_K$  into these more elementary quantities.

In principle one can determine  $\sigma_{xx}$  using conventional, polarization-insensitive spectroscopy techniques such as Kramers-Kronig analysis of reflectance measurements or analysis of transmittance and reflectance measurements. These measurements, however, do not access  $\sigma_{xy}$ , which is critical to understanding many novel materials. Although conventional spectroscopic techniques may be experimentally simpler than the Faraday/Kerr measure-

ments presented in this paper, polarization insensitive approaches to measuring  $\sigma_{xx}$  rely on absolute transmittance and reflectance measurements, which can limit the accuracy of these techniques. On the other hand, since  $\theta_F$  and  $\theta_K$  measurements are absolute measurements that do not require normalization to a reference sample, the accuracy of this technique can be very high. *In this paper, we obtain the entire complex magneto-conductivity tensor by measuring the geometry (orientation axis and ellipticity of the polarization) of reflected and transmitted light; no absolute intensity measurements are required.* A key advantage of determining both  $\sigma_{xx}$  and  $\sigma_{xy}$  from the same set of  $\theta_F$  and  $\theta_K$  measurements is that the behavior of  $\sigma_{xx}$ , which may already be fairly well known, can provide a consistency test for  $\sigma_{xy}$ , which typically is not well known in the MIR. For experimental systems such as ours that are designed for magneto-polarimetry measurements, obtaining  $\sigma_{xx}$  through  $\theta_F$  and  $\theta_K$  measurements is experimentally more straightforward and more accurate than using conventional polarization insensitive spectroscopic techniques.

Of course, this approach has limitations. First, one must sensitively measure polarization changes produced in transmitted and reflected light by a magnetic field. Second, the samples must produce measurable  $\theta_F$  and  $\theta_K$  signals, which is not always the case. For example, in ordinary metals such as Au as well as unconventional metals such as high temperature superconductors  $\theta_K$  is very small and would be difficult to measure accurately. Fortunately, magnetic metals such as SrRuO<sub>3</sub> and Ga<sub>1-x</sub>Mn<sub>x</sub>As produce  $\theta_K$  signals that can be measured readily.

In this paper, we present a MIR polarimetry technique that determines the entire complex conductivity tensor using  $\theta_F$  and  $\theta_K$  measurements. We shall first introduce a sensitive magneto-optical measurement system, next we develop formulas for  $\theta_F$  and  $\theta_K$  in terms of  $\sigma_{xx}$  and  $\sigma_{xy}$ , and finally we shall test these techniques on SrRuO<sub>3</sub> and Ga<sub>1-x</sub>Mn<sub>x</sub>As films.

## II. EXPERIMENTAL SYSTEM

When illuminating a material in a magnetic field using linearly polarized light, the transmitted and reflected beams can be modified in two ways: the plane of polarization can be rotated with respect to the incident linear polarization and the beam may acquire ellipticity. The polarization change of the transmitted light is characterized by the complex Faraday angle  $\theta_F$ , the optical analog of the Hall angle  $\theta_H = \sigma_{xy}/\sigma_{xx}$ , where  $\sigma_{xx}$  is the longitudinal conductivity and  $\sigma_{xy}$  is the transverse (Hall) conductivity.  $\theta_F$  relates the magnitudes and phases of the transmitted electric fields that are perpendicular ( $t_{xy}$ ) and parallel ( $t_{xx}$ ) to the incident linear electric polarization, which is along the  $x$ -direction in this case:  $\tan \theta_F \equiv t_{xy}/t_{xx}$  where  $t_{xx}$  and  $t_{xy}$  are the diagonal and off-diagonal components of the complex magneto-transmission tensor. The complex polar Kerr angle  $\theta_K$  describes the change in the polarization of reflected light for near-normal incidence, with  $\tan \theta_K \equiv r_{xy}/r_{xx}$ , where  $r_{xx}$  and  $r_{xy}$  are the diagonal and off-diagonal components of the complex magneto-reflection tensor. For small changes in the incident polarization,  $\text{Re}(\theta_F)$  ( $\text{Re}(\theta_K)$ ) is related to the rotation and  $\text{Im}(\theta_F)$  ( $\text{Im}(\theta_K)$ ) is related to the ellipticity of the transmitted (reflected) beam's polarization.

The experimental technique used in this paper is based on Ref. 9. There are four new experimental aspects that are added here: 1) precision translational mount for a magneto-optical cryostat; 2) extended wavelength range using additional lasers; 3) reflection measurements to determine  $\theta_K$ ; and 4) new calibration technique. After reviewing the basic experimental technique, this paper will focus on these four new areas. The experimental setup is shown in Fig. 1. The Faraday and Kerr angles are measured using discrete lines from CO<sub>2</sub> (115-133 meV), CO (215-232meV), and HeNe (366 meV) lasers. Measurements have also been made using laser diodes operating at 500 meV and 775 meV located near Lens 3 in Fig. 1. One can probe the samples down to 6 K and magnetic fields up to 7 T in the magneto-optical cryostat. The different laser beams are aligned in one optical path before entering the cryostat (Fig. 1). The original optical path is designed for the

CO<sub>2</sub> laser. The CO laser is sent to probe the sample by inserting mirror  $M_{\text{CO}}$ , which is mounted on a kinematic base before Lens 1. The HeNe laser is sent to probe the sample by inserting mirror  $M_{\text{HeNe}}$ , which is mounted on a kinematic base near the Brewster reflector. An optical chopper modulates the laser intensity with a frequency  $\omega_0$ . To prevent etalon artifacts from multiple reflections within optical components, the cryostat windows and the sample substrate are wedged 1-2°, and the photoelastic modulator (PEM), which is used to analyze the polarization of the transmitted/reflected radiation, is tilted forward 25°. As is discussed in more detail in Section IV B, a compressively strained ZnSe slide produces a well-characterized rotation and ellipticity (see boxed inset in Fig. 1) in the polarization, which can be used to determine the absolute signs of  $\theta_{\text{F}}$  and  $\theta_{\text{K}}$ .

The 7 T magneto-optical cryostat has only two windows, with the sample in vacuum. These room temperature ZnSe windows are placed on 30 cm extension tubes (as can be seen Fig. 2) to minimize their contribution to the Faraday rotation due to the stray magnetic field. The absence of cold windows is important in several respects. First, other magneto-optical cryostat can have up to four cold windows (a pair of liquid helium temperature and a pair of liquid nitrogen temperature windows) that are located close to the sample and therefore experience similar magnetic fields as the sample. Since the cold windows typically are several millimeters thick, they can produce a large magneto-polarization signal that can readily overwhelm the signal produced by the sample, typically several hundred nanometer-thick films. Furthermore, the absence of cold windows increases transmission and reduces artifacts due to multiple reflection.

A photoelastic modulator (PEM) makes it possible to measure sensitively both real and imaginary parts of  $\theta_{\text{F}}$  and  $\theta_{\text{K}}$ .<sup>9</sup> The optical axis of the PEM is oriented vertically along the  $x$  axis and modulates the phase of the transmitted light that is polarized along the  $y$ -direction at a frequency  $\omega_{\text{PEM}}/2\pi \approx 50$  kHz. A linear polarizer  $P_2$  is oriented 45° from vertical and mixes the  $x$  and  $y$  polarization components of the light that has passed through the PEM. A liquid-nitrogen-cooled mercury-cadmium-telluride (MCT) detector measures the intensity of the modulated beam. If the sample does not cause any changes in the

incident polarization, the light entering the PEM is linearly polarized along the  $x$ -direction and there will be no signals at the detector related to the PEM. Three lock-in amplifiers demodulate the detector signal. One lock-in amplifier is referenced to chopper frequency  $\omega_0$  to provide a measurement of the average laser intensity  $I_0$  at the detector. The other two lock-in amplifiers are referenced to harmonics of  $\omega_{\text{PEM}}$  to detect the polarization of the beam. The even harmonics of  $\omega_{\text{PEM}}$  are related to a rotation of the polarization vector [ $\text{Re}(\theta_{\text{F}})$  or  $\text{Re}(\theta_{\text{K}})$ ] and the odd harmonics are related to the ellipticity [ $\text{Im}(\theta_{\text{F}})$  or  $\text{Im}(\theta_{\text{K}})$ ].<sup>9</sup> Typically, one measures the rotation using the second harmonic signal  $I_{2\omega_{\text{PEM}}}$  and the ellipticity using the third harmonic signal  $I_{3\omega_{\text{PEM}}}$ .

The mount holding the 7 T magneto-optical cryostat can be translated with high accuracy ( $\sim 25 \mu\text{m}$ ) both horizontally and vertically. As can be seen in Fig. 2, the cryostat rests on a large 5/16" thick aluminum base plate (17" by 24") that has two long turcrite (grade A, blue) strips attached to the bottom of the base plate directly below the vertical supports. The strips are 0.030" thick, 23" long, and 2" wide, and are epoxied into shallow pockets in the bottom of the plate. Turcrite is optimized for high load, low friction applications and does not cold flow. The base plate and cryostat are moved horizontally with respect to the optical table by turning a 3/8"x24 brass lead screw that is attached to the base plate and the optical table. The height of the cryostat is adjusted by simultaneously turning four 3/4"x16 brass lead screws that are threaded into turcrite bushings in each of the four cryostat mount support legs. To insure that the cryostat is raised and lowered uniformly, without tipping, the brass lead screws are coupled to each other by a 1" wide, 80" long timing belt (T10, 10 mm pitch) that connects 5" diameter timing pulleys that are attached to each lead screw. The design and construction of this mount is challenging since it must be made of non-magnetic materials and since the cryostat weighs approximately 700 pounds. Separate leveling feet at the bottom of each brass lead screw allow the cryostat to be leveled. The magneto-optical signals are critically affected when the probe laser beam is close to the edge of the aperture in the copper plate on which the sample is held, so centering the sample, which can be as small as 3 mm, on the laser beam is very important. Since the lasers are

invisible, this can be difficult. The procedure for centering the sample on the laser beam is greatly improved and simplified using the translating cryostat mount. The transmitted or reflected signal at the detector is simply maximized by translating the sample (along with the cryostat) vertically and horizontally. Precision indicators (shown in Fig. 2) are placed to measure the absolute position of the magneto-optical cryostat. By monitoring the detector signal as one translates the cryostat and sample aperture across the beam, one can determine the laser beam profile and accurately center the sample on the beam. Since they contain magnetic components, the indicators are removed before the running measurements with the superconducting magnet energized. As with the magneto-optical cryostat described in Ref. 9, unwanted motion of the sample is minimized by clamping the lower end of the sample tube to a horizontal delrin rod, which is attached to an aluminum plate in the side window opening of the tailpiece. Furthermore, the tailpiece of the cryostat itself is clamped to the base plate by four bolts that are capped with turcote pads, as shown in Fig. 2. This greatly increases the rigidity of the cryostat mount and minimizes sample movement when the magnetic field is energized.

Unlike Ref. 9, which describes measurements in the 112-136 meV (1100-900  $\text{cm}^{-1}$ ; 11-9  $\mu\text{m}$ ) range, in this paper the measurements have been extended up to 775 meV (6250  $\text{cm}^{-1}$ , 1.6  $\mu\text{m}$ ). Since the PEM, the lenses, and the cryostat windows are ZnSe, the optical system is compatible with sources over the 0.5-20  $\mu\text{m}$  range. The main challenge in using sources with shorter wavelength  $\lambda$  is that the background Faraday rotation due to stray magnetic fields at the windows and sample substrate increases as  $\lambda^{-2}$ .<sup>10</sup> This makes careful measurement and subtraction of the background at shorter wavelengths especially critical. Since this background is reduced when the energy gap of the optical material is increased relative to the photon energy, higher band gap optical materials such as  $\text{BaF}_2$  and  $\text{CaF}_2$  will be used for the cryostat windows in future measurements. A further advantage of  $\text{BaF}_2$  and  $\text{CaF}_2$  is their smaller index (1.5 compared to 2.4 for ZnSe) that reduces Fresnel losses in transmitting light through them. Initially, the 3.4  $\mu\text{m}$  HeNe laser was placed approximately 1.5 m away from the magnet. However the stray magnetic field at that distance induces both rotation

and ellipticity in the output of the HeNe laser that is comparable to the signals produced by many of our samples ( $10^{-3}$  rad at 1 T).<sup>11</sup> This background is dramatically reduced by moving the HeNe laser farther away (2.5 m) from the magneto-optical cryostat.

In this paper both transmission and reflection measurements are made to determine both  $\theta_F$  and  $\theta_K$ , whereas only transmission measurements ( $\theta_F$ ) were reported in Ref. 9. Although  $\theta_F$  and  $\theta_K$  provide similar information, there are several advantages to measuring both. First, in the metallic films that are reported here, the transmittance can be very low as is discussed in the Section III of this paper. The reflectance amplitudes, on the other hand, are typically on the order of 50 % or higher. Although the substrates used in our measurements are relatively transparent in the MIR,  $\theta_K$  measurements are not limited to transparent substrates and can even be applied to bulk materials where transmission measurements would be impossible for metals. The fact that  $\theta_F$  and  $\theta_K$  are related is also an advantage in that the self-consistency of the results may be confirmed.

In Ref. 9 we describe several techniques to calibrate the polarimetry system. We have developed a new technique which allows the simultaneous calibration of the PEM retardance  $R_{\text{PEM}}$  and the angle  $\alpha_2$  of the final linear polarizer  $P_2$ . One of the calibration techniques in Ref. 9 is to rotate the PEM by a known small angle  $\phi$  and use the change in the normalized detector signal  $S_2$  that is at  $2\omega_{\text{PEM}}$  to calibrate  $\theta_F$ . The PEM and polarizer  $P_2$  are rotated as a single unit, so that the angle  $\alpha_2$  between the PEM and  $P_2$  is kept constant. In this case, we measure the normalized signals  $S_2$  and  $S_4$  at  $2\omega_{\text{PEM}}$  and  $4\omega_{\text{PEM}}$ , respectively. For  $\phi \ll 1$  these signals depend on  $\phi$  as follows:

$$S_2 = \frac{I_{2\omega_{\text{PEM}}}}{I_0} = \frac{4J_2(R_{\text{PEM}})\phi \tan(\alpha_2)}{1 + J_0(R_{\text{PEM}})\phi \tan(\alpha_2)} \quad (1)$$

$$S_4 = \frac{I_{4\omega_{\text{PEM}}}}{I_0} = \frac{4J_4(R_{\text{PEM}})\phi \tan(\alpha_2)}{1 + J_0(R_{\text{PEM}})\phi \tan(\alpha_2)} \quad (2)$$

$$\frac{S_2}{S_4} = \frac{J_2(R_{\text{PEM}})}{J_4(R_{\text{PEM}})} \quad (3)$$

where  $J_n$  are  $n$ th order Bessel functions,  $I_0$  is the signal at the chopper frequency,  $I_{2\omega_{\text{PEM}}}$  is the signal at  $2\omega_{\text{PEM}}$ , and  $I_{4\omega_{\text{PEM}}}$  is the signal at  $4\omega_{\text{PEM}}$ . Note that the ratio of  $S_2$  and  $S_4$  in

Eq. 3 only depends on  $R_{\text{PEM}}$ , as all the other factors cancel. One can use the measurement of  $S_2/S_4$  to determine  $R_{\text{PEM}}$ . Since neither  $\phi$  nor  $\alpha_2$  enter into Eq. 3, this calibration is not affected by the amount the PEM is rotated, as long  $\phi \ll 1$ , nor by the precise orientation of polarizer  $P_2$ . Once  $R_{\text{PEM}}$  is determined, it can be entered into either Eqs. 2 or 3 to determine  $\alpha_2$ , which is nominally  $45^\circ$ . Although  $\alpha_2$  can be calibrated, when doing measurements at a various wavelengths, errors can be reduced by keeping  $\alpha_2$  constant. The errors in adjusting  $P_2$  to make  $\alpha_2 = 45^\circ$  at each wavelength can be significant. If  $\alpha_2$  is kept constant, there will be no variation from wavelength to wavelength due to different settings of  $P_2$ . A further check when performing this calibration at different wavelengths and different lasers, is that  $\alpha_2$  from the fits should be the same since  $P_2$  was not moved with respect to the PEM. In our calibration measurements,  $\alpha_2$  determined from this calibration typically remains constant to within  $0.2^\circ$  over the entire measurement range. As in Ref. 9, the roll-off attenuation of the detector and its associated electronics is included in the final calibration. We have found that the roll-off also depends on the gain setting of the detector pre-amplifier.

### III. SAMPLES

The  $\text{SrRuO}_3$  sample consists of a 282 nm thick  $\text{SrRuO}_3$  film on a  $\text{LaSrGaO}_4$  substrate and was grown by pulsed laser deposition at Oak Ridge National Laboratory as described in Ref. 12. The  $\text{LaSrGaO}_4$  substrate is transparent in the MIR, which allowed **both** transmission and reflection measurements to be made. The thickness of the  $\text{SrRuO}_3$  film and the fact that the substrate begins to absorb strongly below 117 meV, resulted in transmittances that could be below 0.01 %. Fortunately, high power coherent sources such as the  $\text{CO}_2$  and CO lasers coupled with a liquid nitrogen cooled detector provide the measurement system with the necessary dynamic range to measure small changes in the polarization even for such small transmittance values. The back of the  $\text{LaSrGaO}_4$  substrate was polished to a  $2^\circ$  wedge after the film was grown.

The  $\text{Ga}_{1-x}\text{Mn}_x\text{As}$  sample having a Curie temperature of 95 K was synthesized using  $\text{Mn}^+$

ion implantation followed by pulsed-laser melting (II-PLM).<sup>13,14</sup> A semi-insulating GaAs (001) wafer was implanted with 80 keV Mn<sup>+</sup> to a dose of  $1.8 \times 10^{16}$  cm<sup>-2</sup> and irradiated in air with a single 0.4 J/cm<sup>2</sup> pulse from a KrF excimer laser. The total Mn concentration depth profile measured by secondary ion mass spectrometry (SIMS) was nearly Gaussian with a peak value of approximately 8 % and a width of 50 nm. The back of the GaAs substrate was polished to a 1° wedge after the film was grown.

#### IV. ANALYSIS

Although many experimental improvements have been made since our first report in Ref. 9, the primary contribution of this paper involves a novel analysis of  $\theta_F$  and  $\theta_K$  measurements. In this section we develop thick-film formulas for  $\theta_F$  and  $\theta_K$  in terms of  $\sigma_{xx}$  and  $\sigma_{xy}$ . We also discuss the sign conventions that are used for  $\theta_F$  and  $\theta_K$ .

##### A. Thick-film equations for $\theta_F$ and $\theta_K$

Since  $\theta_F$  and  $\theta_K$  are defined in terms of the complex transmission and reflection amplitudes  $t_{xy}$ ,  $t_{xx}$ ,  $r_{xy}$ , and  $r_{xx}$ , we begin by determining these amplitudes. As light passes through a thick film sample on a wedged substrate, part of the beam is reflected and part is transmitted at each interface, as shown in Fig. 3. The beam that reflects off the first air-film interface combines with beams that have been multiply reflected within the film to produce the reflected light. Since the back of the substrate is wedged, beams that reflect from it do not combine with the beams reflecting off the film. The first pass beam combines with beams that are multiply reflected within the film to produce the transmitted light entering the substrate. This transmitted light is also multiply reflected within the substrate, but since the substrate is wedged, each order of reflection exits the substrate at a different angle. Therefore, the main advantage of using a wedged substrate is that one can spatially separate the first-pass beam from beams that are multiply reflected within the substrate.

Consider a thick film with complex index of refraction  $n_f$  on a wedged substrate with

complex index of refraction  $n_s$ . The Fresnel coefficients  $t_{ij}$  and  $r_{ij}$  describe the transmission and reflection amplitudes, respectively, at each interface separating a material with index  $n_i$  from a material with index  $n_j$ . Summing over all transmitted beams including only multiple reflections within the film, the complex transmission coefficient for the sample is given by:

$$t(n_f) = \frac{t_{0f}t_{fs}e^{i\phi_f}}{1 - r_{fs}r_{f0}e^{2i\phi_f}}t_{s0}e^{i\phi_s} = \frac{2}{(1 + n_s) \cos(kd) - i(n_f + \frac{n_s}{n_f}) \sin(kd)}t_{s0}e^{i\phi_s}, \quad (4)$$

where  $k = \omega n_f/c$  is the wave number of the light within the film and  $d$  is the thickness of the film. The index 0 represents air. The phase shift of beam that passes through the film is given by  $\phi_f = kd$ . For the wedged substrate, we are only interested in the first pass beam, which experiences a phase shift of  $\phi_s = (\omega n_s d_{\text{sub}})/c$ , where  $d_{\text{sub}}$  is the thickness of wedged substrate.

Similarly adding all contributions to the reflected light, the total reflection coefficient becomes:

$$r(n_f) = \frac{r_{0f} + r_{fs}e^{2i\phi_f}}{1 - r_{fs}r_{f0}e^{2i\phi_f}} = \frac{(n_s - 1) \cos(kd) - i(n_f - \frac{n_s}{n_f}) \sin(kd)}{(1 + n_s) \cos(kd) - i(n_f + \frac{n_s}{n_f}) \sin(kd)}. \quad (5)$$

Note that the  $r(n_f)$  on a wedged substrate is the same as for a film on an infinitely thick substrate since the reflection from the back of the substrate never reaches the detector.

The following calculation connects the  $\theta_F$  to the optical conductivities  $\sigma_{xx}$  and  $\sigma_{xy}$ . We shall assign the  $z$ -axis as the direction of light propagation and also the direction of the magnetic field  $B$ . Assuming that the sample is cylindrically symmetric along  $z$ -axis, the conductivity tensor would be indistinguishable between  $x$ - and  $y$ -axis,  $\sigma_{xx} = \sigma_{yy}$  and  $\sigma_{xy} = -\sigma_{yx}$ . Therefore, the optical conductivity tensor is purely diagonal in the circular polarization basis. One can write the complex dielectric function  $\varepsilon_{\pm}$  for a circularly polarized basis with either positive or negative helicity.  $\varepsilon_{\pm}$  is related to the conductivity  $\sigma_{\pm}$ , represented in the circular basis, by

$$\varepsilon_{\pm} = \varepsilon_b - \frac{4\pi}{i\omega}\sigma_{\pm} = \varepsilon_b - \frac{4\pi}{i\omega}(\sigma_{xx} \pm i\sigma_{xy}) = \varepsilon_0 \mp \frac{4\pi}{\omega}\sigma_{xy}, \quad (6)$$

where  $\varepsilon_b$  is the response of bound charges and  $\varepsilon_0 \equiv \varepsilon_b - 4\pi\sigma_{xx}/i\omega$  is the longitudinal component of dielectric function. The complex index of refraction  $n_{f,\pm}$  for the film using a circular polarization basis can be expressed in terms of  $\varepsilon_{\pm}$  and  $\sigma_{xy}$ .

$$n_{f,\pm} = \sqrt{\varepsilon_{\pm}} = \sqrt{\varepsilon_0} \left( 1 \mp \frac{\sigma_{xy}}{\sigma_b + i\sigma_{xx}} \right)^{1/2}, \quad (7)$$

where  $\sigma_b$  is defined as  $\frac{\omega}{4\pi}\varepsilon_b$ . Since  $\sigma_{xx} \gg \sigma_{xy}$  in most cases in the MIR,  $n_{f,\pm}$  can be simplified to

$$n_{f,\pm} \simeq \sqrt{\varepsilon_0} \mp \frac{1}{2} \sqrt{\varepsilon_0} \frac{\sigma_{xy}}{\sigma_b + i\sigma_{xx}} = n_{f,0} \mp \delta n_f, \quad (8)$$

where  $n_{f,0} = \sqrt{\varepsilon_0}$  is longitudinal component of complex index of refraction and  $\delta n_f = 2\pi\sigma_{xy}/\omega n_{f,0}$  is the transverse component. The diagonal (longitudinal) transmission coefficient  $t_{xx}$  and the off-diagonal (transverse) transmission coefficient  $t_{xy}$  in a linear polarization basis are related to the diagonal transmission coefficients  $t_+$  and  $t_-$  in the circular polarization basis as follows. Since  $t_{\pm}(n_{f,\pm}) \approx t_0(n_{f,0}) \pm (\partial t_0/\partial n_{f,0})\delta n_f$ ,

$$t_{xx} = \frac{t_+ + t_-}{2} \approx t_0(n_{f,0}), \quad (9)$$

$$t_{xy} = \frac{t_+ - t_-}{2i} \approx \frac{1}{i} \left( \frac{\partial t_0}{\partial n_{f,0}} \right) \delta n_f. \quad (10)$$

Equations (9) and (10) show that diagonal transmission measurements probe the sum of  $t_+$  and  $t_-$ , whereas off-diagonal transmission measurements, e.g., Faraday measurements, probe the difference, making them more sensitive to small changes in  $t_+$  and  $t_-$  induced by magnet fields or other symmetry-breaking mechanisms. Putting Eqs. (9) and (10) together, the Faraday angle  $\theta_F$  can be represented in terms of  $\sigma_{xy}$  and  $\sigma_{xx}$  (found in  $n_{f,0}$ ) as

$$\tan \theta_F = \frac{t_{xy}}{t_{xx}} = -i\delta n_f \frac{1}{t_0(n_{f,0})} \frac{\partial t_0}{\partial n_{f,0}} = \frac{-2\pi i}{\omega n_{f,0}} \left( \frac{1}{t_0(n_{f,0})} \frac{\partial t_0}{\partial n_{f,0}} \right) \sigma_{xy}. \quad (11)$$

One can use the complex transmission coefficient  $t_0(n_{f,0})$  (Eq. (4)) to calculate the Faraday

angle  $\theta_F$ .

$$\tan \theta_F = \left( \frac{-2\pi i \sigma_{xy}}{\omega n_{f,0}} \right) \frac{\left[ (1 + n_s) \left( \frac{\omega d}{c} \right) + i \left( 1 - \frac{n_s}{n_{f,0}^2} \right) \right] \sin(kd) + i \left( n_{f,0} + \frac{n_s}{n_{f,0}} \right) \left( \frac{\omega d}{c} \right) \cos(kd)}{(1 + n_s) \cos(kd) - i \left( n_{f,0} + \frac{n_s}{n_{f,0}} \right) \sin(kd)}. \quad (12)$$

Taking the approximation  $kd = (2\pi d)/\lambda \ll 1$  ( $d \rightarrow 0$ ,  $\omega \rightarrow 0$ ), the Eq. (12) yields the simple thin-film formula

$$\tan \theta_F \approx \left( \frac{\sigma_{xy}}{\sigma_{xx}} \right) \left[ 1 + \frac{1}{Z_+ \sigma_{xx}} \right]^{-1}, \quad (13)$$

where  $Z_{\pm} \equiv (Z_0 d)/(n_s \pm 1)$ ,  $Z_0$  is the impedance of free space and the unit of conductivity is  $\Omega^{-1} \text{ cm}^{-1}$ . Note that Eq. (13) is slightly different from Eq. (2.2) in Ref. 15 due to a typographical error on the right side of Eq. (2.2).

One can use the same approach to calculate  $\theta_K$  in terms of  $\sigma_{xx}$  and  $\sigma_{xy}$  using the reflection coefficients. The diagonal and the off-diagonal reflection amplitudes,  $r_{xx}$  and  $r_{xy}$ , can be expressed in a linear polarization basis in terms of the diagonal reflection coefficients  $r_+$  and  $r_-$  in the circular polarization basis.

$$r_{xx} = \frac{r_+ + r_-}{2} \approx r_0(n_{f,0}), \quad (14)$$

$$r_{xy} = \frac{r_+ - r_-}{2i} = \frac{1}{i} \left( \frac{\partial r_0}{\partial n_{f,0}} \right) \delta n_f. \quad (15)$$

Again, we have assumed that  $r_{\pm}(n_{f,\pm}) \approx r_0(n_{f,0}) \pm (\partial r_0 / \partial n_{f,0}) \delta n_f$ . Combining Eq. (14) and Eq. (15) produces an expression for  $\theta_K$  in terms of  $\sigma_{xx}$  and  $\sigma_{xy}$ ,

$$\tan \theta_K = \frac{r_{xy}}{r_{xx}} = -i \delta n_f \frac{1}{r_0(n_{f,0})} \frac{\partial r_0}{\partial n_{f,0}} = \frac{-2\pi i}{\omega n_{f,0}} \left( \frac{1}{r_0(n_{f,0})} \frac{\partial r_0}{\partial n_{f,0}} \right) \sigma_{xy}. \quad (16)$$

To calculate the Kerr angle  $\theta_K$ , we can use the complex reflection coefficient  $r_0$  (Eq. (5)).

$$\begin{aligned} \tan \theta_K &= \left( \frac{-2\pi i \sigma_{xy}}{\omega n_{f,0}} \right) \frac{\left[ -(n_s - 1) \left( \frac{\omega d}{c} \right) - i \left( 1 + \frac{n_s}{n_{f,0}^2} \right) \right] \sin(kd) - i \left( n_{f,0} - \frac{n_s}{n_{f,0}} \right) \left( \frac{\omega d}{c} \right) \cos(kd)}{(n_s - 1) \cos(kd) - i \left( n_{f,0} - \frac{n_s}{n_{f,0}} \right) \sin(kd)} \\ &+ \left( \frac{-2\pi i \sigma_{xy}}{\omega n_{f,0}} \right) \frac{\left[ (n_s + 1) \left( \frac{\omega d}{c} \right) + i \left( 1 - \frac{n_s}{n_{f,0}^2} \right) \right] \sin(kd) + i \left( n_{f,0} + \frac{n_s}{n_{f,0}} \right) \left( \frac{\omega d}{c} \right) \cos(kd)}{(n_s + 1) \cos(kd) - i \left( n_{f,0} + \frac{n_s}{n_{f,0}} \right) \sin(kd)} \quad (17) \end{aligned}$$

Applying the same approximation ( $kd \ll 1$ ) used for  $\theta_F$  to Eq. (17) results in the thin-film formula for  $\theta_K$ ,

$$\tan \theta_K \approx \left( \frac{\sigma_{xy}}{\sigma_{xx}^2} \right) \left( -\frac{2}{Z_0 d} \right) \left[ \left( 1 + \frac{1}{Z_+ \sigma_{xx}} \right) \left( 1 + \frac{1}{Z_- \sigma_{xx}} \right) \right]^{-1}, \quad (18)$$

where the unit of conductivity is  $\Omega^{-1} \text{ cm}^{-1}$ .

Equations (11) and (16) can be simplified by using the relation between  $\sigma_{xx}$  and  $n_{f,0}$  obtained by the Eqs. (6) and (8).

$$\begin{aligned} \tan \theta_F &= -\frac{1}{t_0} \left( \frac{\partial t_0}{\partial \sigma_{xx}} \right) \sigma_{xy}, \\ \tan \theta_K &= -\frac{1}{r_0} \left( \frac{\partial r_0}{\partial \sigma_{xx}} \right) \sigma_{xy}. \end{aligned} \quad (19)$$

Note that since both  $\tan \theta_F$  and  $\tan \theta_K$  are proportional to  $\sigma_{xy}$ , the magneto-optical signals vanish when  $\sigma_{xy} = 0$ , as expected. Dividing  $\tan \theta_F$  in Eq. (11)  $\tan \theta_K$  in Eq. (16) allows  $\sigma_{xy}$  to divide out and produces

$$\frac{\tan \theta_F}{\tan \theta_K} = \frac{\frac{1}{t_0} \left( \frac{\partial t_0}{\partial n_{f,0}} \right)}{\frac{1}{r_0} \left( \frac{\partial r_0}{\partial n_{f,0}} \right)} = F(n_{f,0}). \quad (20)$$

Also, it can be expressed as

$$\frac{\tan \theta_F}{\tan \theta_K} = \frac{\frac{1}{t_0} \left( \frac{\partial t_0}{\partial \sigma_{xx}} \right)}{\frac{1}{r_0} \left( \frac{\partial r_0}{\partial \sigma_{xx}} \right)} = G(\sigma_{xx}). \quad (21)$$

Since  $\delta n_f \ll n_{f,0}$ ,  $t_0 \approx t_{xx}$  and  $r_0 \approx r_{xx}$  in the linear polarization basis, and the complex function  $F(n_{f,0})$  only depends on the longitudinal index of refraction of the film. If the complex  $\theta_F$  and  $\theta_K$  are measured experimentally, one can solve Eq. (20) numerically to obtain  $n_{f,0}$ . Once  $n_{f,0}$  is determined, we can use Eqs. (6) and (8) to calculate the complex longitudinal conductivity  $\sigma_{xx}$  of the film:

$$\sigma_{xx} = \frac{i\omega}{4\pi} (\varepsilon_b - n_{f,0}^2), \quad (22)$$

where  $\varepsilon_b$  is the contribution to the dielectric function from bound carriers, which allows the conductivity to be determined for free carriers. In these measurements, we typically are

interested in the response of all the carriers, bound and free, so  $\varepsilon_b$  is set to 0. Using the measured values for  $\theta_F$  or  $\theta_K$ , and plugging  $n_{t,0}$  back into Eqs. (11) or (16), one can now determine the complex  $\sigma_{xy}$ .

## B. Sign calibration

The sign calibration is important for our Faraday and Kerr measurements because the solutions for  $\sigma_{xx}$  and  $\sigma_{xy}$  depend on which signs are assigned to  $\theta_F$  and  $\theta_K$ . There are two sign conventions in describing the time-evolution of the electric field in magneto-optical measurements:  $\exp(-i\omega t)$  or  $\exp(+i\omega t)$ . Determining the correct signs for  $\theta_F$  and  $\theta_K$  can be challenging, both experimentally and theoretically.

Experimentally, one must make sure that the direction of the magnetic field is known and that the direction of the changes in orientation and ellipticity in the polarization of the transmitted and reflected light are properly determined. Since the signals are demodulated using lock-in amplifiers, one must keep track of the phase of each lock-in in order to avoid sign errors.

In our measurements the signs of the polarization signals are determined in three independent, yet overlapping, ways. The sign of the polarization rotation ( $\text{Re}(\theta_F)$  and  $\text{Re}(\theta_K)$ ) is determined by rotating the PEM and linear polarizer  $P_2$  together in a counter-clockwise direction as viewed along the beam's propagation direction towards the detector. This is equivalent to the sample rotating the transmitted/reflected polarization in the clockwise direction. The change in signal is compared with that produced by the sample in a magnetic field. Second, the sign of both the rotation and ellipticity can be verified by placing a ZnSe slide in the beam as described in Refs. 9,16. The index of refraction in ZnSe is decreased for the linear polarization along the compressive strain direction,<sup>17</sup> and hence this polarization exits the ZnSe slide before the polarization that is perpendicular to the compressively strained axis. For the geometry shown in the boxed inset of Fig. 1, this phase shift between perpendicular linear polarizations produces a counterclockwise rotation of the

linear polarization as well as a counterclockwise ellipticity, as viewed towards the detector. The strain on the ZnSe slide is applied by hanging a weight on a compression lever, as can be seen in greater detail in Ref. 16. Since the orientation of the slide critically affects the transmitted polarization, the slide holder is clamped to the optical table to prevent small movements of the slide when the weight is added or removed. The same calibration can be made using a waveplate, as described in Ref. 9, but a ZnSe slide is much less expensive than a zeroth order infrared waveplate, and since the strain is applied externally, there is no ambiguity for the direction of the fast axis, which is not always clear on a waveplate. The compressed slide sign calibration technique can be used over a large wavelength range (500 nm to 20  $\mu\text{m}$ ) without any sign changes for two reasons: 1) the strain, and therefore the retardance, of the slide is small, so even at the shortest wavelengths in this range the retardance never approaches  $\pi$ , where fast and slow axes would reverse. 2) the piezobirefringence coefficient for ZnSe does not change sign in this wavelength range.<sup>17</sup> These sign calibrations are performed with the sample in place and under exactly the same conditions that are used for measuring the sample. Once the calibrations are completed, the PEM is aligned with the laser polarization and the ZnSe slide is removed before the magnetic field is energized. Once the directions of the rotation and ellipticity signals are determined with respect to the magnetic field direction and the direction of light propagation, one can use Ref. 18 to determine the proper signs of  $\theta_F$  and  $\theta_K$ .

Finally, the signs of polarization signals are verified by measuring  $\text{Re}(\theta_F)$  and  $\text{Im}(\theta_F)$  produced by a gold film at 120 meV. Since  $\theta_F$  in gold is produced by free electrons, one can characterize the response of a sample in  $\text{Re}(\theta_F)$  and  $\text{Im}(\theta_F)$  as “electron-like” or “hole-like.” One can represent the complex  $\sigma_{xx}$  and  $\sigma_{xy}$  of gold using a simple Drude model, which in turn can be used to calculate  $\theta_F$  using the thick-film transmission formula in Eq. (11). This same formula is then used to calculate “backwards” from the measured  $\theta_F$  and  $\theta_K$  produced by other samples to obtain  $\sigma_{xx}$  and  $\sigma_{xy}$ . The signs of  $\text{Re}(\theta_F)$  and  $\text{Im}(\theta_F)$  determined by this calculation can be used to determine the signs produced by other samples. For example, applying Eq. (11) to a Drude model for a gold film produces  $\text{Re}(\theta_F) < 0$  and  $\text{Im}(\theta_F) < 0$

below 200 meV. Therefore, if the  $\text{Re}(\theta_F)$  signal for a sample has the same polarity with applied magnetic field as the signal from a gold film (electron-like), a negative value of  $\text{Re}(\theta_F)$  is used in the thick-film equation to determine  $\sigma_{xx}$  and  $\sigma_{xy}$ . The sign of  $\text{Im}(\theta_F)$  is determined the same way. This convention insures that a film with an electron-like response in both  $\text{Re}(\theta_F)$  and  $\text{Im}(\theta_F)$  will produce the correct signs and magnitudes of  $\sigma_{xx}$  and  $\sigma_{xy}$ . Since  $\theta_K$  from a gold film is too small to measure, we cannot use the gold film to calibrate the sign of  $\theta_K$ .

The signs obtained using these three techniques are all consistent with each other. For example, rotating the PEM counter-clockwise produced a signal with the opposite polarity as applying strain to the ZnSe slide. Furthermore, the signs (determined by rotating the PEM or straining a ZnSe slide) of the transmitted polarization signals produced by a gold film were consistent with the lower frequency ( $< 200$  meV) behavior of electrons in a magnetic field.

When the calibrated signs for the measured  $\theta_F$  and  $\theta_K$  are used in our thick film equations, we obtain reasonable optical properties. First, the real  $n$  and imaginary  $k$  parts of the index of refraction are positive. Second, for probe frequencies below the plasma frequency of metallic samples such as Au and SrRuO<sub>3</sub>, the real part of the dielectric function  $\epsilon_1 = n^2 - k^2$  is negative, implying that  $n < k$ . The final signs for  $\sigma_{xx}$  and  $\sigma_{xy}$  are not arbitrarily assigned, but are determined from the measurements and the calibration procedure described here.

## V. RESULTS

The measurements on the SrRuO<sub>3</sub> and Ga<sub>1-x</sub>Mn<sub>x</sub>As films reported here probe the anomalous Hall effect, which is the Hall effect that arises from the sample magnetization. Therefore, to eliminate contributions from the ordinary Hall effect, which depends on the applied magnetic field, these measurements were performed on films that are fully magnetized out of plane with zero applied magnetic field. In the case of Ga<sub>1-x</sub>Mn<sub>x</sub>As where the remanent magnetization was very small, the finite-field linear behavior is extrapolated back to  $B = 0$ .<sup>19</sup>

The measurement and analysis techniques described in this paper can be applied to finite magnetic fields equally well.

Figure 4 shows  $\theta_F$  and  $\theta_K$  at 10 K and 0 T from the SrRuO<sub>3</sub> film with the sample fully magnetized out of plane as a function of probe energy  $E$ .  $\theta_F$  and  $\theta_K$  exhibit strong energy dependence, with  $\text{Re}(\theta_F)$  and  $\text{Im}(\theta_K)$  changing sign at 250 meV and 130 meV, respectively. Below 300 meV, both  $\text{Re}(\theta_F)$  and  $\text{Im}(\theta_F)$  are negative, indicating that the change in polarization is in the same sense as the Faraday signals from free electrons in a gold reference film. Strictly speaking,  $\theta_F$  and  $\theta_K$  are not defined at zero energy, but they approach well-defined values as  $E \rightarrow 0$ . The dc values of  $\theta_F$  and  $\theta_K$  in Fig. 4 are determined using the thick film equations (Eqs. (11) and (16)) as  $E \rightarrow 0$  with the dc measurements for  $\sigma_{xx}$  and  $\sigma_{xy}$ . The dc  $\theta_H$  at 10 K and 0 T with the sample fully magnetized is  $-0.0052$  rad, which is within 2% of  $\theta_F(E \rightarrow 0)$  and confirms the expected relationship for metallic materials where  $\theta_F \approx \theta_H$  as frequency goes to zero.<sup>15</sup> The  $\theta_F$  and  $\theta_K$  signals from SrRuO<sub>3</sub> are significantly larger than what has been measured in non-magnetic metals. For example, in gold, copper, and HTSC films, where the Faraday signals are produced by free carriers in a magnetic field,  $\text{Re}(\theta_F) \approx \text{Im}(\theta_F) \approx 0.001$  rad at 8 T.<sup>15,20</sup>

The inset of Fig. 4 shows  $\theta_F$  and  $\theta_K$  from the SrRuO<sub>3</sub> film as a function of applied magnetic field at a probe energy of 117 meV at 10 K. The response of  $\theta_F$  to the applied magnetic field is electron-like, as determined by comparing the signals to a gold film reference sample. Although the intensity of transmitted light can be as small as 0.01 %, the magneto-optical signals in transmission ( $\theta_F$ ) are approximately an order of magnitude larger than those obtained in reflection ( $\theta_K$ ). This is due to the fact that in metallic films  $\theta_F \propto \sigma_{xy}/\sigma_{xx}$  while  $\theta_K \propto \sigma_{xy}/(\sigma_{xx})^2$ , as is suggested by Eqs. 13 and 18. Therefore, for highly metallic films in the MIR, where  $\sigma_{xx} \gg \sigma_{xy}$ ,  $\theta_F$  is typically larger than  $\theta_K$  for the same  $\sigma_{xy}$ .

Figure 5 shows the measured complex a) longitudinal conductivity  $\sigma_{xx}$  and b) transverse conductivity  $\sigma_{xy}$  for the SrRuO<sub>3</sub> film. The large symbols are obtained from  $\theta_F$  and  $\theta_K$  measurements at 10 K and 0 T with the sample fully magnetized out of plane. The signs of  $\sigma_{xx}$  and  $\sigma_{xy}$  represented by the symbols are not assigned arbitrarily, but are determined

experimentally using the techniques described in Section IV B. The conductivity was defined to include contributions from both bound and free charges, although the bound charge contribution in the MIR was found to be small and had almost no effect on the results. The heavy solid ( $\text{Re}(\sigma_{xx})$ ) and dashed ( $\text{Im}(\sigma_{xx})$ ) lines in a) are from  $H = 0$  Kramers-Kronig analysis of reflectance measurements at 35 K and 0 T on a different SrRuO<sub>3</sub> film by Z. Schlesinger's group.<sup>21</sup> The qualitative agreement between the  $\sigma_{xx}$  obtained by  $\theta_F$  and  $\theta_K$  measurements and that obtained by reflectance measurements is excellent over the entire energy range. The quantitative differences could be readily accounted for by the differences in the two samples, especially since the sample measured by the Schlesinger group had a dc resistivity at 10 K of approximately  $20 \mu\Omega \text{ cm}$ ,<sup>3,21</sup> a factor of three smaller than the resistivity of the sample used in the  $\theta_F$  and  $\theta_K$  measurements. The complex  $\sigma_{xx}$  obtained using  $\theta_F$  and  $\theta_K$  measurements can be compared with values determined by transmittance and reflectance measurements on the same sample (small symbols with error bars in Fig. 5a). In the 117-224 meV range,  $\sigma_{xx}$  obtained using  $\theta_F$  and  $\theta_K$  measurements is within 20 % of the average values obtained using transmittance and reflectance measurements. At 366 meV the average difference is closer to 30 % due to the difficulty in aligning the weak HeNe laser, which has an output of 2 mW that is two order of magnitude lower than the CO<sub>2</sub> and CO lasers. Furthermore, the differences in the quality of the polish of the wedged sample and reference substrates are much more critical at this shorter wavelength. At all wavelengths,  $\sigma_{xx}$  obtained by Faraday and Kerr measurements is within the error bars of  $\sigma_{xx}$  obtained using transmittance and reflectance measurements. Challenges in absolute transmission and reflection measurements using discrete laser lines on a wedged sample could easily account for the differences and suggest that in this case  $\theta_F$  and  $\theta_K$  measurements, which are self-normalizing, may allow a more accurate determination of  $\sigma_{xx}$ .

Figure 6 shows  $\theta_F$  and  $\theta_K$  at 10 K and 0 T from the Ga<sub>1-x</sub>Mn<sub>x</sub>As film with the sample fully magnetized out of plane as a function of probe energy.  $\theta_F$  and  $\theta_K$  show strong energy dependence, including sign changes.  $\theta_F$  and  $\theta_K$  exhibit qualitatively similar behavior in this case.

Figure 7 shows the measured complex a) longitudinal conductivity  $\sigma_{xx}$  and b) transverse conductivity  $\sigma_{xy}$  for the  $\text{Ga}_{1-x}\text{Mn}_x\text{As}$  film. These were obtained from  $\theta_F$  and  $\theta_K$  measurements at 10 K and 0 T with the sample fully magnetized out of plane. The  $E = 0$  results are from dc magnetotransport measurements by the Dubon group on similar samples also grown by them. The symbols with error bars in Fig. 7a) shows  $\sigma_{xx}$  obtained from transmittance and reflectance measurements. Since it was more difficult to obtain an optically smooth polish on GaAs (compared to  $\text{LaSrGaO}_4$ ), and perhaps because it has a larger index of refraction (compared to  $\text{LaSrGaO}_4$ ), differences in the quality of the GaAs substrate polish led to more than a factor of two uncertainty in the transmittance at 366 meV due to scattering. Therefore, transmittance and reflectance measurements at 366 meV and shorter wavelengths are not included. The quality of the polish made no measurable impact at the longer wavelengths. Since the Faraday and Kerr measurements involve changes in polarization with applied magnetic field, substrate roughness did not measurably affect the accuracy of the  $\theta_F$  and  $\theta_K$  measurements. The transmittance and reflectance measurements led to a  $\sigma_{xx}$  that qualitatively agrees with the  $\sigma_{xx}$  obtained by Faraday and Kerr measurements, which was within the error bars of the transmittance and reflectance measurements.

The magnitude and frequency dependence of  $\sigma_{xx}$  compares reasonably well with results from other experiments and from theoretical models. The MIR  $\text{Re}(\sigma_{xx})$  extrapolates smoothly to the dc  $\sigma_{xx}$ .  $\text{Re}(\sigma_{xx})$  is similar to that obtained in Refs. 22 and 23 for  $\text{Ga}_{1-x}\text{Mn}_x\text{As}$  samples. The frequency dependence of  $\text{Re}(\sigma_{xx})$  is also similar to that predicted by theoretical models.<sup>6,7</sup> One can also represent the complex conductivity in terms of the complex dielectric constant  $\epsilon$ . In this case, the  $\text{Re}(\epsilon)$  remains at a fairly constant value of 9 over the measured frequency range whereas  $\text{Im}(\epsilon)$  strongly decreases with increasing energy as  $E^{-1.3}$ , reaching a value of approximately 3 at 0.76 eV. This compares well with ellipsometry measurements on  $\text{Ga}_{1-x}\text{Mn}_x\text{As}$  films where  $\text{Re}(\epsilon)$  levels off at a value between 10 and 12 as  $E \rightarrow 0$ , while  $\text{Im}(\epsilon)$  is close 2 at 0.75 eV and begins to rise as  $E \rightarrow 0$ .<sup>24</sup> Note that the negative sign in  $\text{Im}(\sigma_{xx})$  in Fig. 7a) is consistent with the positive  $\text{Re}(\epsilon)$  found in ellipsometry measurements in the MIR. The reasonable behavior of  $\sigma_{xx}$  in Fig. 7a) provides

added confidence that the  $\sigma_{xy}$  found in Fig. 7b) accurately represents the response of the  $\text{Ga}_{1-x}\text{Mn}_x\text{As}$  film. The MIR  $\text{Re}(\sigma_{xy})$  extrapolates smoothly to the dc  $\sigma_{xy}$ . Note that the low energy behavior of the  $\text{Re}(\sigma_{xy})$  is hole-like, suggesting that there is no sign reversal in the AHE between 0 and 100 meV.

## VI. CONCLUSION

We have demonstrated experimental and analytical techniques that can be used to determine the complete complex magneto-conductivity tensor from Faraday and Kerr measurements in ferromagnetic metals and semiconductors. It is interesting to note that no absolute intensity measurements are required; the polarization of the reflected and transmitted light is sufficient to completely determine the complex magneto-conductivity tensor. In both  $\text{SrRuO}_3$  and  $\text{Ga}_{1-x}\text{Mn}_x\text{As}$  films,  $\sigma_{xx}$  obtained using Faraday and Kerr measurements was quantitatively consistent with the values for  $\sigma_{xx}$  that were obtained using conventional transmittance and reflectance measurements. Furthermore, in both materials,  $\sigma_{xy}$  showed strong spectral features, including peaks and sign changes, which will be discussed in future papers. With the increasing application of magneto-optical measurements to study magnetic and non-magnetic materials, and with the specific interest in the infrared longitudinal and transverse conductivity of magnetic oxides and semiconductors, these techniques may have a significant impact in a number of fields.

### Acknowledgments

We wish to thank H.D. Drew for his thick film transmission calculation, D.C. Schmadel for his advice in constructing our strained ZnSe polarization sign calibrator, and K. Cullinan for his work on designing and machining the translating mount for the magneto-optical cryostat. We also thank J.S. Dodge for his helpful discussions and John Kielkopf for introducing turcite to us. This work was supported by Research Corporation Cottrell Scholar Award (Buffalo), NSF-CAREER-DMR0449899 (Buffalo), NSF-DMR-0554796 (Santa Cruz), and DOE Con-

tract No. DE-AC03-76SF00098 (Berkeley). Research at Oak Ridge National Laboratory was sponsored by the Division of Materials Sciences and Engineering, Office of Basic Energy Sciences, U.S. Department of Energy, under Contract No. DE-AC05-00OR22725 with Oak Ridge National Laboratory, managed and operated by UT-Battelle, LLC.

---

- <sup>1</sup> J.M. Harris, Y.F. Yan, and N.P. Ong, *Phys. Rev. B* **46**, 14293 (1992).
- <sup>2</sup> H. Ohno, H. Munekata, Y. Penney, S. von Molnar, and L.L. Chang, *Phys. Rev. Lett.* **68**, 2664 (1992).
- <sup>3</sup> L. Klein, J. S. Dodge, C. H. Ahn, G. J. Snyder, T. H. Geballe, M. R. Beasley, and A. Kapitulnik, *Phys. Rev. Lett.* **77**, 2774 (1996).
- <sup>4</sup> Y. Kats, I. Genish, L. Klein, J.W. Reiner, and M. R. Beasley, *Phys. Rev. B* **70**, 180407(R)1-4 (2004).
- <sup>5</sup> Z. Fang, N. Nagaosa, K. S. Takahashi, A. Asamitsu, R. Mathieu, T. Ogasawara, H. Yamada, M. Kawasaki, Y. Tokura, and K. Terakura, *Science* **302**, 92-95 (2003).
- <sup>6</sup> J. Sinova, T. Jungwirth, J. Kucera, and A. H. MacDonald, *Phys. Rev. B* **67**, 235203/235201-235212 (2003).
- <sup>7</sup> E. M. Hankiewicz, T. Jungwirth, T. Dietl, C. Timm, and Jairo Sinova, *Phys. Rev. B* **70**, 245211 (2004).
- <sup>8</sup> A. Zimmers, L. Shi, D. C. Schmadel, W. M. Fisher, R. L. Greene, H. D. Drew, M. Houseknecht, G. Acbas, M.-H. Kim, M.-H. Yang, J. Cerne, J. Lin, and A. Millis, cond-mat/0510085 also submitted to *Phys. Rev. B, Rapid Comm.*, 2007.
- <sup>9</sup> J. Cerne, D. C. Schmadel, L. Rigal, and H. D. Drew, *Rev. Sci. Instr.* **74**, 4755-4767 (2003).
- <sup>10</sup> G. Ruymbeek, W. Grevendonk, and P. Nagels, *Physica* **89B**, 14 (1977).
- <sup>11</sup> H. Bedi, Master's Thesis, University at Buffalo, SUNY, 2006.
- <sup>12</sup> P. Khalifah, I. Ohkubo, H. Christen, and D. Mandrus, *Phys. Rev. B* **70**, 134426 (2004).
- <sup>13</sup> M. A. Scarpulla, O. D. Dubon, K. M. Yu, O. Monteiro, M. R. Pillai, M. J. Aziz, and M. C. Ridgway, *Appl. Phys. Lett.* **82**, 1251-1253 (2003).
- <sup>14</sup> M. A. Scarpulla, U. Daud, K.M Yu, O. Monteiro, Z. Liliental-Weber, D. Zakharov, W. Walukiewicz, and O. D. Dubon, *Physica B* **340-342**, 908-912 (2003).

- <sup>15</sup> J. Černe, D.C. Schmadel, M. Grayson, G.S. Jenkins, J. R. Simpson, and H. D. Drew, *Phys. Rev. B* **61**, 8133 (2000).
- <sup>16</sup> D.C. Schmadel, "The ac Hall effect in single crystal bismuth strontium calcium copper oxide," Ph.D. Dissertation, University of Maryland, College Park, MD, USA. Avail. UMI, Order No. DA3080294. (2002).
- <sup>17</sup> P.Y. Yu and M. Cardona, *J. Phys. Chem. Solids* **34**, 29-56 (1973).
- <sup>18</sup> R. Atkinson and P.H. Lissberger, *Applied Optics* **31**, No. 28, 6076 (1992).
- <sup>19</sup> G. Acbas, J. Černe, M. Cukr, V. Novak, and J. Sinova, International Conference on the Physics of Semiconductors, 28th, Vienna, July 24-28, 2006, 1217-1219 (2007).
- <sup>20</sup> J. Černe, M. Grayson, D.C. Schmadel, G.S. Jenkins, H. D. Drew, R. Hughes, A. Dabkowski, J.S. Preston, and P.-J. Kung, *Phys. Rev. Lett.* **84**, 3418 (2000).
- <sup>21</sup> P. Kostic, Y. Okada, N.C. Collins, Z. Schlesinger, J. W. Reiner, L. Klein, A. Kapitulnik, T. H. Geballe, and M. R. Beasley, *Phys. Rev. Lett.* **81**, 2498 (1998).
- <sup>22</sup> K. S. Burch, D. B. Shrekenhamer, E. J. Singley, J. Stephens, B. L. Sheu, R. K. Kawakami, P. Schiffer, N. Samarth, D. D. Awschalom, and D. N. Basov, *Phys. Rev. Lett.* **97**, 087208 (2006).
- <sup>23</sup> E. J. Singley, K. S. Burch, R. Kawakami, J. Stephens, D. D. Awschalom, and D. N. Basov, *Phys. Rev. B* **68**, 165204 (2003).
- <sup>24</sup> K. S. Burch, J. Stephens, R. K. Kawakami, D. D. Awschalom, and D. N. Basov, *Phys. Rev. B* **70**, 205208 (2004).

## Figures

FIG. 1: Overall schematic of the optical path. The polarization change induced by compressively straining a ZnSe slide is shown in the boxed inset.

FIG. 2: The mount that allows the 700 pound magneto-optical cryostat (labeled 1 in figure) to be translated vertically and horizontally with  $\sim 25 \mu\text{m}$  precision. The knob (9) attached to the lead screw (10) for horizontal translation is indicated in the left part of the photograph. Vertical adjustment is made by pulling on the timing belt (5), which rotates the four timing pulleys (4) simultaneously, causing the large brass lead screws (3) to move the support legs (2) up or down.

FIG. 3: Optical path of light passing through a thick film on a wedged substrate. The multiply reflected beams in film are drawn at non-normal angles for clarity.

FIG. 4: Energy dependence of a)  $\theta_F$  and b)  $\theta_K$  from a SrRuO<sub>3</sub> film with the sample fully magnetized perpendicular to the plane at 0 T and 10 K. Since the measurement is at  $H = 0$  T, the OHE as well as background signals from the substrate and windows, which are linear in  $H$ , do not contribute to the signal. Note the strong energy dependence and the sign changes in  $\text{Re}(\theta_F)$  and  $\text{Im}(\theta_K)$  at 250 K and 130 meV, respectively. The  $\theta_F(E \rightarrow 0)$  plotted in a) is determined using Eq. 13 with the dc measurements for the dc  $\theta_H$  and  $\sigma_{xx}$ . Inset shows the relationship between  $\text{Re}(\theta_F)$ ,  $\text{Im}(\theta_F)$ , and  $\text{Re}(\theta_K)$  (which is multiplied by a factor of 5) at 117 meV and 10 K.

FIG. 5: The longitudinal conductivity  $\sigma_{xx}$  a) and transverse (AHE) conductivity  $\sigma_{xy}$  b) for a SrRuO<sub>3</sub> film as a function of probe energy. The solid symbols are obtained from  $\theta_F$  and  $\theta_K$  measurements at 10 K and 0 T with the sample fully magnetized out of plane. The smaller symbols with error bars in a) are determined from conventional transmittance and reflectance measurements of the same SrRuO<sub>3</sub> film. The heavy solid ( $\text{Re}(\sigma_{xx})$ ) and dashed ( $\text{Im}(\sigma_{xx})$ ) lines in a) are from Kramers-Kronig analysis of reflectance measurements at 35 K and 0 T on a different SrRuO<sub>3</sub> sample by Z. Schlesinger's group.

FIG. 6: Energy dependence of the AHE a)  $\theta_F$  and b)  $\theta_K$  from a  $\text{Ga}_{1-x}\text{Mn}_x\text{As}$  film with the sample fully magnetized perpendicular to the plane at 0 T and 10 K. Note the strong energy dependence and the sign changes in both the real and imaginary parts of  $\theta_F$  and  $\theta_K$ .  $\theta_F$  and  $\theta_K$  exhibit qualitatively similar behavior in this case.

FIG. 7: The longitudinal conductivity  $\sigma_{xx}$  a) and transverse (AHE) conductivity  $\sigma_{xy}$  b) from a  $\text{Ga}_{1-x}\text{Mn}_x\text{As}$  film as a function of probe energy. The measurements are at 10 K and 0 T with the sample fully magnetized out of plane. The smaller symbols with error bars in a) are determined from conventional transmittance and reflectance measurements of the same  $\text{Ga}_{1-x}\text{Mn}_x\text{As}$  film. The  $E = 0$  results are from dc measurements by the Dubon group on similar samples, which were also grown them.

Fig. 1

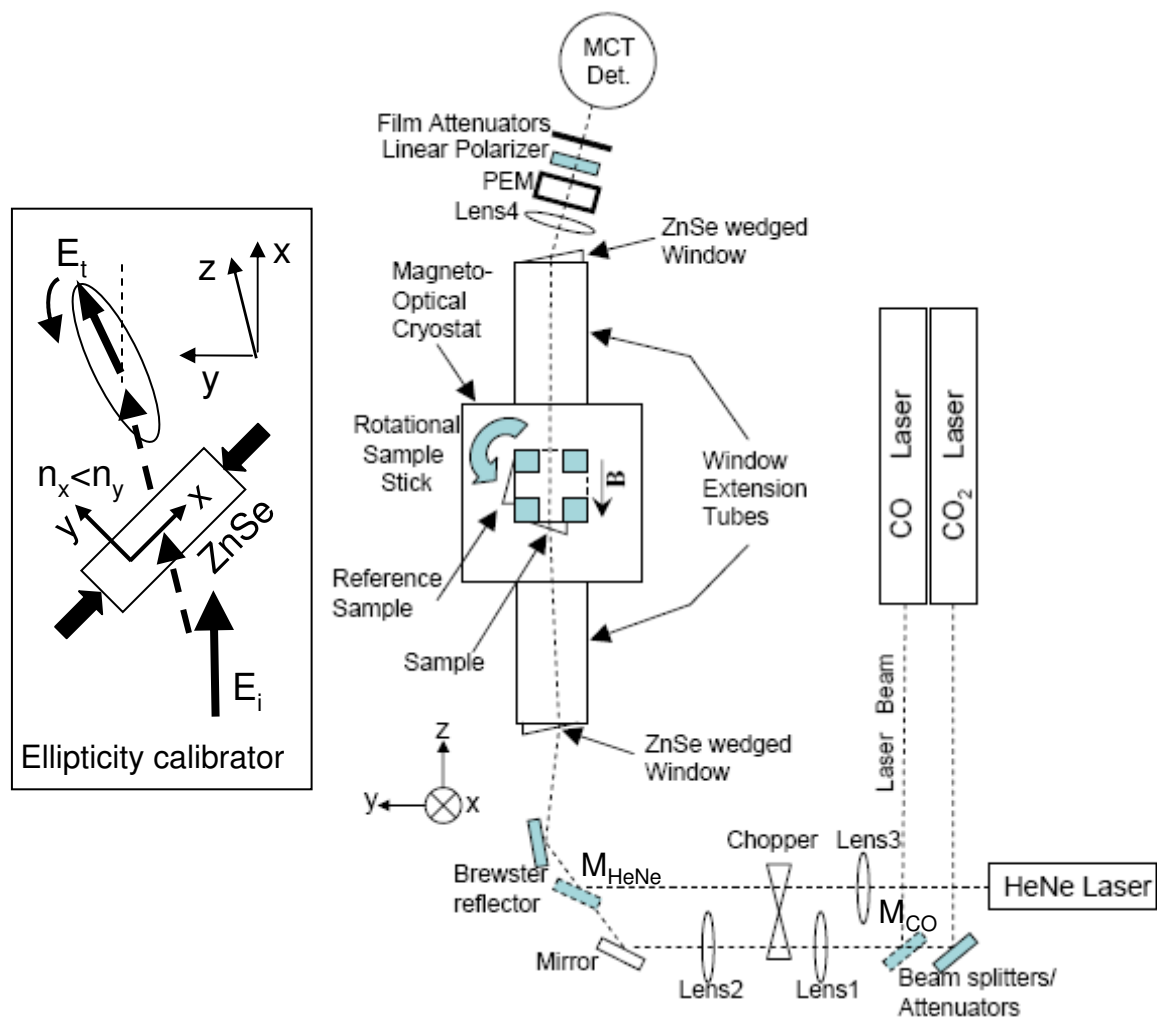
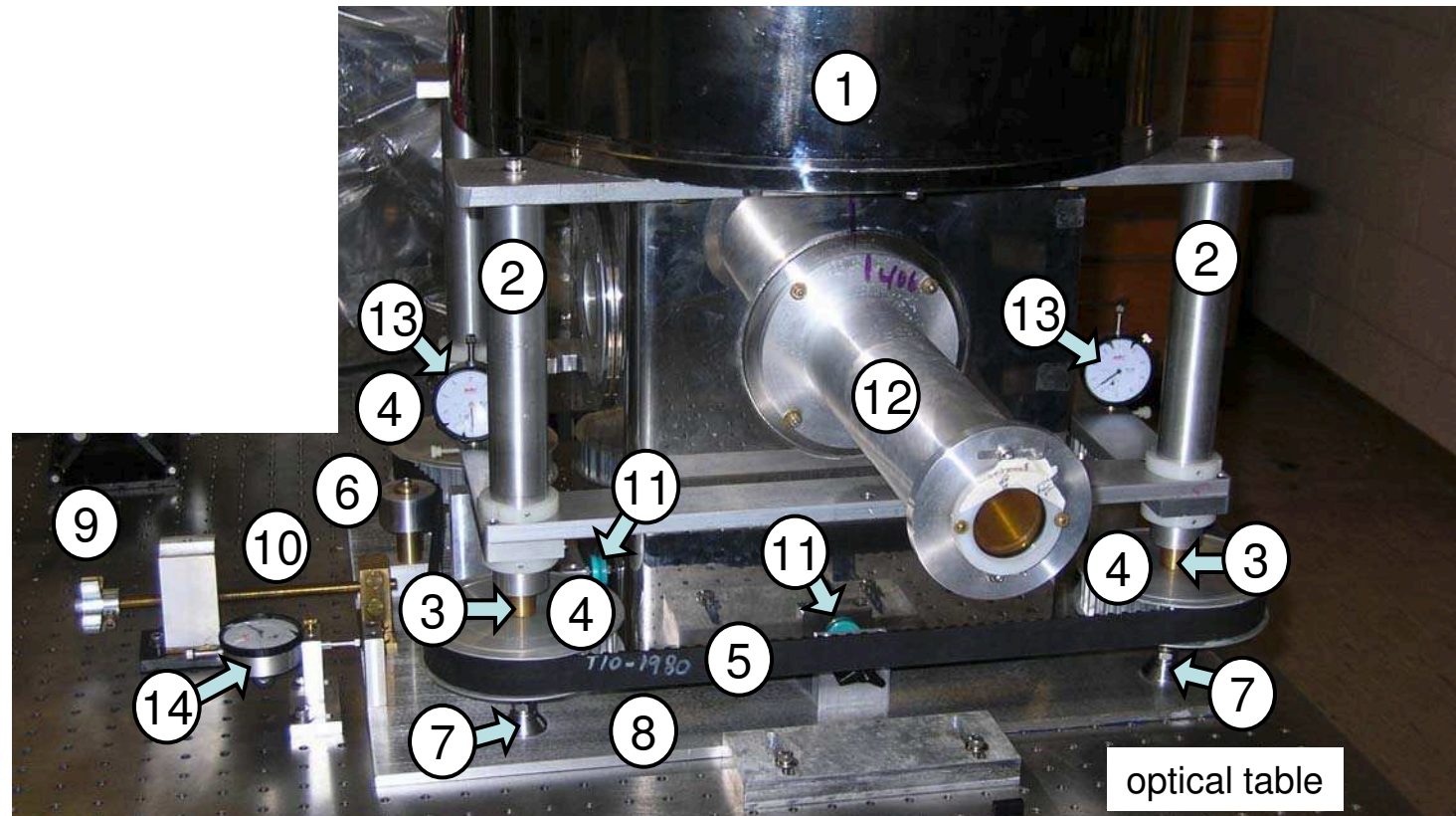


Fig. 2



1. 7 T magneto-optical cryostat	6. belt tensioning pulley	11. tailpiece clamps (4)
2. alum. mount support legs (4)	7. leveling feet (4)	12. window extension tube
3. brass vertical lead screws (4)	8. alum. base plate	13. vert. position indicator
4. alum. timing pulleys (4)	9. horiz. adjustment knob	14. horiz. position indicator
5. timing belt	10. brass horiz. lead screw	

